Proceedings of ASME Turbo Expo 2014: Turbine Technical Conference and Exposition
GT2014
June 16 – 20, 2014, Düsseldorf, Germany

GT2014-25876

LARGE EDDY SIMULATION OF A HIGH PRESSURE TURBINE STAGE: EFFECTS OF SUB-GRID SCALE MODELING AND MESH RESOLUTION

Dimitrios Papadogiannis *
Florent Duchaine
Frédéric Sicot
Laurent Gicquel
CFD team
CERFACS
42 ave Gaspard Coriolis
31057, Toulouse, France
Email: dimitrios.papadogiannis@cerfacs.fr

Gaofeng Wang
Stéphane Moreau
Département de Génie Mécanique
University of Sherbrooke
Sherbrooke, Québec, J1K 2R1
Canada

ABSTRACT

The use of Computational Fluid Dynamics (CFD) tools for integrated simulations of gas turbine components has emerged as a promising way to predict undesired component interactions thereby giving access to potentially better engine designs and higher efficiency. In this context, the ever-increasing computational power available worldwide makes it possible to envision integrated massively parallel combustion chamber-turbomachinery simulations based on Large-Eddy Simulations (LES). While LES have proven their superiority for combustor simulations, few studies have employed this approach in complete turbomachinery stages. The main reason for this is the known weaknesses of near wall flow modeling in CFD. Two approaches exist: the wall-modeled LES, where wall flow physics is modeled by a law-of-the-wall, and the wall-resolved LES where all the relevant near wall physics is to be captured by the grid leading to massive computational cost increases. This work investigates the sensitivity of wall-modeled LES of a high-pressure turbine stage. The code employed, called TurboAVBP, is an in-house LES code capable of handling turbomachinery configurations. This is possible through an LES-compatible approach with the rotor/stator interface treated based on an overset moving grids method. It is designed to avoid any interference with the numerical scheme, allow the proper representation of turbulent structures crossing it and run on massively parallel platforms. The simulations focus on the engine-representative MT1 transonic high-pressure turbine, tested by QinetiQ. To control the computational cost, the configuration employed is composed of 1 scaled stator section and 2 rotors. The main issues investigated are the effect of mesh resolution and the effect of sub-grid scale models in conjunction with wall modeling. The pressure profiles across the stator and rotor blades are in good agreement with the experimental data for all cases. Radial profiles at the rotor exit (in the near and far field) show improvement over RANS predictions. Unsteady flow features, inherently present in LES, are, however, found to be affected by the modeling parameters as evidenced by the obtained shock strengths and structures or turbulence content of the different simulations.

NOMENCLATURE

$\mathbf{W}$	Conservative variables vector
$\vec{\mathscr{F}}^C$	Convective fluxes
$\vec{\mathscr{F}}^V$	Viscous fluxes
p	Pressure
T	Temperature
ρ	Density
r	Mixture gas constant
ν_τ	Turbulent viscosity

---

*Address all correspondence to this author.

Δ Filter width
$\tilde{\mathbf{S}}$ Resolved rate-of-strain tensor
$\tilde{\mathbf{g}}$ Resolved velocity gradient tensor
σ Singular values of velocity gradient tensor
CFD Computational Fluid Dynamics
LES Large Eddy Simulation
(U)RANS (Unsteady) Reynolds Averaged Navier-Stokes

INTRODUCTION

In recent years, the use of Computational Fluid Dynamics (CFD) methods has become prevalent in the design of gas turbines. With the new engines targeting higher efficiency, higher power-to-weight ratios, increased reliability and compliance to strict emissions and noise regulations (see ACARE Vision 2020), the need for highly accurate simulation tools has increased significantly. In parallel, with severe weight restrictions more and more applicable, industrial focus has oriented towards integrated simulations of the engine components, since most gas turbine instabilities usually occur from interactions between different parts of the engine. The combustion chamber-turbine interaction is of particularly important, since the turbine inlet temperature is one of the key parameters determining the overall efficiency of the gas turbine cycle and the accurate prediction of the aerothermal flow field with any unsteady phenomena, notably hot-streaks arriving from the combustor, is highly desired.

Current industrial state-of-the-art in turbomachinery simulations usually relies in solving the Reynolds Averaged Navier-Stokes (RANS) equations with some turbulence modeling to calculate the mean variables of the stationary flow field. If unsteady flow features are to be captured, the prevalent method is performing Unsteady RANS (URANS) simulations [1]. While both these methods are mature and with an affordable computational cost, they are subject to several limitations. They do not explicitly resolve any turbulent length scales and show deficiencies in predicting transition and flow separation [2]. This is very restrictive for turbomachinery flows, where there are complex flow phenomena, including boundary layer transitions, flow separations and reattachments [1], vortex shedding and high levels of free-stream turbulence [3, 4].

Large Eddy Simulations (LES), able to resolve a large range of the turbulent spectrum with an unsteady formulation, are promising for turbomachinery applications. However, due to the high computational cost associated with wall resolved LES (Chapman [5] evaluated it to be scaling approximately with $Re^{1.8}$, where Re is the Reynolds number) and the weaknesses in wall modeling, only few studies have been performed so far in this field. Most of the investigated configurations are cascades of blades, or slices of the full 3D blade, of both low and high Reynolds numbers [4, 6–10]. Results are in good agreement with the experiments and show improvement over RANS. The main advantages of LES over (U)RANS appear on the prediction of unsteady phenomena (notably laminar to turbulent transition, flow separation bubbles and blade wake profiles) and secondary flows, which are shown to be among the most important loss inducing mechanisms [11].

Recently, with the latest generation of supercomputers in place, LES studies of complete turbomachinery stages, including the critical part of rotor/stator interaction, emerge. Gourdain performed wall-resolved LES (up to 1 billion points) of the entire CME2 compressor stage [12]. LES was not only capable of predicting the mean flow variables but also provided information on turbulent structures and frequencies not present in URANS simulations. Additionally, the laminar-turbulent transition is captured accurately, an important advantage of LES. Similar conclusions are drawn by McMullan et al [13], who performed LES on 2 different compressor stage configurations. Their results show good agreement with the available experimental data and highlight the importance of free-stream turbulence and inlet boundary conditions in the development of the flow field. Regarding turbine stages, Wang et al [14] performed LES of the high-pressure turbine MT1 using coupled instances of the reactive unstructured LES solver AVBP [15]. An overset grid method was developed for the interface treatment between the stator and rotor. Despite being relatively under-resolved, the predicted flow field is close to that measured in the experimental bench and rich secondary flow structures are revealed.

Both previous studies rely on wall-resolved LES. So far, there has been no investigation on the effects of mesh resolution and sub-grid scale models used in wall-modeled LES of turbomachinery stages. The effect of Sub-Grid Scale (SGS) models, in particular, can be significant, since turbine flows are wall dominated, high Reynolds number flows with several boundary layers interacting with each other, strong gradients and vortical structures. This makes wall-modeled LES of such flows particularly challenging. Evaluating the sensitivity of the flow field to the mesh resolution, as well as the effect of SGS modeling in conjunction with a law-of-the-wall, is important to allow a degree of confidence on the results. This study builds on the work of Wang et al [14] and looks into these two areas by performing several similar LES of the high-pressure turbine stage MT1. The MT1 turbine is a full scale research turbine that was tested in the frame of the European project TATEF-II [16]. It has also been the subject of several numerical studies using traditional RANS solvers [17, 18]. These previous investigations form a large database for validation and comparison with the LES approach of Wang et al [14] in a realistic configuration.

EXPERIMENTAL SET-UP

The experiments used to validate this study were conducted at the Oxford Turbine Research Facility. The testing bench is a short duration, rotating and isentropic light piston wind tunnel designed for investigating turbine stages. It has the ability to create engine representative test conditions for turbines up to one and a half stages. Both aerodynamic and heat transfer measurements can be performed simultaneously at a moderate cost. More details on the installation and the function of the facility are provided by Hilditch et al [19].

The investigated turbine configuration is the MT1 high-pressure turbine. It is an unshrouded, single stage, high-pressure experimental turbine designed by Rolls-Royce. It is a full scale turbine and works in engine representative conditions, forming a database for the validation of numerical methods in a realistic configuration. The stage consists of 32 stator and 60 rotor blades. The experimental data include inlet and exit area surveys of total pressure, azimuthally averaged rotor exit profiles in the near and far field, profiles of the isentropic Mach number across the stator blade at three different spanwise positions, as well as the pressure profile across the rotor at mid span [16]. Finally, Qureshi et al [20] provide additional experimental information on the secondary flow structures across the rotor blades.

COMPUTATIONAL METHOD

Governing equations

The governing equations of the flow across a turbine stage are the unsteady, compressible Navier-Stokes equations, which describe the mass, momentum and energy conservation. It is often convenient to express them in conservative form as:

$$\frac{\partial \mathbf{W}}{\partial t} + \vec{\nabla} \cdot \vec{\mathscr{F}} = 0, \tag{1}$$

where $\mathbf{W}$ is the vector containing the conservative variables $(\rho, \rho\mathbf{U}, \rho E)^T$ and $\vec{\mathscr{F}} = (\mathbf{F}, \mathbf{G}, \mathbf{H})^T$ is the flux tensor. For convenience, the flux is divided into two components:

$$\vec{\mathscr{F}} = \vec{\mathscr{F}}^C(\mathbf{W}) + \vec{\mathscr{F}}^V(\mathbf{W}, \nabla\mathbf{W}) \tag{2}$$

where $\vec{\mathscr{F}}^C$ is the convective flux depending on $\mathbf{W}$ and $\vec{\mathscr{F}}^V$ is the viscous flux depending on both $\mathbf{W}$ and its gradients $\nabla\mathbf{W}$. The fluid follows the perfect gas law $p = \rho r T$, with r being the mixture gas constant. The dynamic viscosity varies with temperature according to a power law.

The principle of LES is to separate the largest turbulent length scales present in the flow, that can be resolved by the mesh, from the smaller scales through a low-pass filtering of the Navier-Stokes equations. The effect of the unresolved small scales appears through the unresolved sub-grid scale tensor, which is commonly modeled using the Boussinesq assumption [21]. This assumption relates the unresolved scales with the resolved rate-of-strain and the turbulent viscosity, calculated by an SGS model.

Sub-grid scale models

While trying to model the unresolved scales, SGS operators are not perfect and might not follow certain universal flow properties and erroneously introduce additional turbulent viscosity. A primary one is that turbulence stresses are damped near the walls, thus turbulent viscosity should follow the same behavior (named property P1). Additionally, two other desired properties are that turbulent viscosity should be zero in case of pure shear and pure rotation (property P2) as well as when there is isotropic or axisymmetric contraction/expansion (property P3) [22].

Satisfying property P1 is essential in wall-resolved LES. It is less constraining with a law-of-the-wall, which attempts to model the near-wall behavior. However, SGS models can also affect the matching region [23] and the outer boundary layer, where wall modeling by classic analytic law-of-the-walls is not applicable. Thus, the choice of the SGS model can still have a large impact on the flow field. In this study, the effects of three SGS models in turbomachinery fluid flows are analyzed: the classic Smagorinsky [24], the Wall Adapting Local-Eddy viscosity (WALE) model [25], which is one of the most commonly used in wall-bounded flows, and the recent σ model [22].

Table 1 summarizes which of the desired properties are satisfied by the formulation of the three SGS models.

	Smagorinsky	**WALE**	σ
P1	NO	YES	YES
P2	NO	NO	YES
P3	NO	NO	YES

TABLE 1: Summary of the three sub-grid scale models, their constants and whether they satisfy the desired properties

Smagorinsky model

The Smagorinsky model [24] is the simplest SGS model for LES. It has the advantages of being easy to implement and robust. It is often used in conjunction with wall modeling. The formula for ν_τ writes:

$$\nu_\tau = (C_S \Delta)^2 \sqrt{2\tilde{S}_{ij}\tilde{S}_{ij}} \tag{3}$$

In Eq. (3) Δ is the filter width and C_S is the Smagorinsky coefficient, equal to 0.18.

Wall Adapting Local Eddy-viscosity model (WALE)

Developed by Nicoud et al [25], WALE aims at capturing the change of scales close to walls without using a dynamic approach (Germano [26]). The turbulent viscosity reads:

$$\nu_\tau = (C_w\Delta)^2 \frac{(s^d_{ij}s^d_{ij})^{3/2}}{(\tilde{S}_{ij}\tilde{S}_i j)^{5/2} + (s^d_{ij}s^d_{ij})^{5/4}} \qquad (4)$$

with s^d_{ij} being:

$$s^d_{ij} = \frac{1}{2}(\tilde{g}^2_{ij} + \tilde{g}^2_{ji}) - \frac{1}{3}\tilde{g}^2_{kk}\delta_{ij} \text{ with } \tilde{g}_{ij} = \frac{\partial \tilde{u}_i}{\partial x_j}, \qquad (5)$$

C_w is the coefficient of the WALE model, equal to 0.5.

σ model

The σ model, developed by Nicoud et al [22], attempts to satisfy all the above mentioned properties P1-P3. Instead of being based on the strain rate tensor, its operator is formulated based on the singular values $(\sigma_1, \sigma_2, \sigma_3)$ of the velocity gradient tensor:

$$\nu_\tau = (C_\sigma\Delta)^2 \mathscr{D}_\sigma \text{ with } \mathscr{D}_\sigma = \frac{\sigma_3(\sigma_1 - \sigma_2)(\sigma_2 - \sigma_3)}{\sigma_1^2}, \qquad (6)$$

where $C_\sigma = 1.5$. It is the most recently developed of all the models employed, hence its capacity in handling more complex configurations has not been tested.

Overset grid method for the rotor/stator interface

To extend the capabilities of the available LES solver and deal with rotor/stator simulations, external code coupling is preferred. Hence two or more copies of the same LES solver, each with their own computational domain, are coupled through the parallel coupler OpenPALM [27]. The developed method is called Multi Instances Solvers Coupled via Overlapping Grids (MISCOG). The whole flow domain is initially divided into static (Domain01) and rotating parts (Domain02) (as shown in Fig. 1). For rotating parts, the code uses the moving-mesh approach [28] in the absolute frame of reference while the remaining unit simulates the flow in the non-rotating part in the same coordinate system. The difficulty lies in the accurate exchange of the information crossing the interface. This is handled through an overset grid method. The MISCOG method consists of reconstructing the residuals at the interface through exchanges and linear interpolation (2nd order accurate) of the conservative variables. It has been validated extensively on a set of canonical cases, to ensure minimal disturbance of the information crossing the interface and preservation of the accuracy of the numerical scheme [14]. The numerical schemes available are the Lax-Wendroff [29], which is second order in space and time, as well as TTG4A and TTGC [30], which are third order in time and space. All of the schemes are explicit in time. During this study only the second order Lax-Wendroff scheme is employed. Higher order interpolation is under development to permit use of the higher order schemes.

SIMULATION SET-UP

The MT1 turbine, consisting of 32 stator and 60 rotor blades, allows for the periodic simulation of a quarter of the 360 degrees annulus (8 stators and 15 rotors). In an effort to reduce the computational cost, the ”reduced blade count” technique is employed, also used in previous simulations of the MT1 turbine [17, 31]. This technique involves scaling the blades in order to change the actual blade count, while keeping the same operating point. Salvadori et al [17] scaled the rotor blade, increasing the blade count to 64, hence reducing their domain to a periodic simulation of one stator and two rotor passages. Hosseini et al [18] performed numerical simulations of the MT1 turbine using different blade counts and concluded that the impact of scaling on the mean aerodynamic flow field is insignificant, as long as solidity is maintained. The disadvantage of this method is that the unsteady flow field and secondary flows will be impacted. In this study, contrary to previous publications, a small scaling is performed in the stator and the final blade count is 30:60, hence creating a periodic domain of 12 degrees. More aggressive scalings are possible but the chosen blade count allows a minimal disturbance of the principal flow frequencies while rendering parametric studies affordable. The distance of the inflow location to the stator is approximately a quarter of the stator chord length, while the distance from the rotor trailing edge to the outlet is two rotor chord lengths.

Mesh generation

Two different meshes are employed in this study. They are fully 3D hybrid meshes, with prism layers around the blades and tetrahedral elements in the vane and endwalls. Figure 1 provides an overview of the coarsest mesh, while Table 2 summarizes the main characteristics of the meshes. The coarse mesh (MESH1) is composed of 8.1 million cells in total for the stator domain and 10.5 million cells for the rotor domain. It is designed to place the first nodes around the blade walls in the logarithmic region of a turbulent boundary layer, hence allowing for law-of-the-wall to be used effectively while reducing the computational cost. Note also that the prisms have a low aspect ratio set to $\Delta x^+ \approx 4\Delta y^+ \approx 4\Delta z^+$, permitting good resolution of streamwise/spanwise flow structures. The fine mesh (MESH2) is designed to improve the overall resolution and place nodes deeper in the boundary layers to evaluate the effect of the turbulent structures formed in the outer and logarithmic parts. It has an aspect ratio of the prisms increased to $\Delta x^+ \approx 10\Delta y^+ \approx 10\Delta z^+$ to reduce the computational cost. In the rotor tip region the coarsest mesh

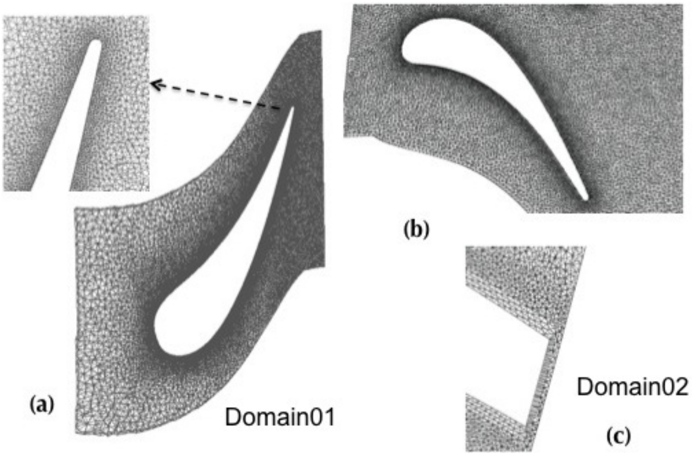

FIGURE 1: MESH VIEW OF THE STATOR (a), ROTOR (b) AND ROTOR TIP (c) MESH

has only 6-7 cell layers, shown in Fig. 1c, rendering the resolution rather limited in that area, in an effort to keep the mesh cell count limited. Nonetheless, You et al [32] showed that mesh resolution is crucial for accurate predictions of the tip leakage vortices. The fine mesh (MESH2) has approximately 17 layers of cells, allowing for a much better representation of the secondary flows developing in the tip clearance.

In wall units, the maximum values of $y+$ measured with meshes range from 130, for MESH1, and 15, for MESH2, both of these located around the stator blade. It is noted that the endwalls are not as well resolved as the blades of each mesh.

	MESH1	**MESH2**
Stator cell count	8.1M	40M
Rotor cell count	10.5M	74M
Stator/Rotor prism layers	1/4	10/10
Max y+	130	15
$\frac{\Delta x+}{\Delta y+} = \frac{\Delta z+}{\Delta y+}$	4	10

TABLE 2: MAIN PROPERTIES OF THE GENERATED MESHES

Boundary Conditions

The boundary conditions follow the NSCBC formulation [33] and consist of imposing a total pressure and total temperature for the inlet and a static pressure at the outlet. The values imposed are those of the experiment. Imposing the total pressure and temperature as an inlet has the advantage of allowing a natural inflow velocity profile, since experimental measurements of the inlet profiles were not possible. No turbulent fluctuation is imposed, because information on the turbulence intensity and length scales of the incoming flow field are unavailable. Regarding the outlet condition, the NSCBC conditions have been shown to naturally permit the development of the radial pressure gradient due to the radial equilibrium [34]. The walls in the experiments are isothermal. However, the numerical simulation are performed using adiabatic walls, therefore not allowing the development of the thermal boundary layers and, consequently, heat flux predictions at the blade walls. The poor near wall resolution for the coarse mesh does not permit accurate heat flux predictions, hence adding isothermal walls would unnecessarily increase the complexity of the parametric studies. All boundary conditions are summarized in Table 3.

Boundary conditions of the MT1 high-pressure turbine

Rotational Speed (rpm)	9500
Inlet total pressure (Pa)	$4.56 * 10^5$
Inlet total temperature (K)	444
Mass flow (kg/sec)	17.4
Outlet static pressure (Pa)	$1.4 * 10^5$

TABLE 3: SUMMARY OF THE BOUNDARY CONDITIONS

Cases investigated

This study follows two different axes. First, a study on the effect of the SGS models is performed. For this reason, three different cases are computed, all employing the coarse MESH1. The SGS models evaluated are the Smagorinsky model (Case 1), the WALE model (Case 2) and the σ model (Case 3). The computational cost for a full rotation of the turbine stage is 6k CPU hours (approximately 2 days on 128 cores). The second axis is focused on identifying the effect of mesh resolution on the flow predictions. For this part, the fine mesh (MESH2) is employed with two different SGS models, the classic Smagorinsky and the WALE model, which are considered the most mature models for complex geometries. Note that wall modeling is used throughout. A summary of the cases investigated and their respective characteristics and cost (in CPUHours) can be found in Table 4. It is evident that the increase in resolution leads to a large increase of the computational cost, due to increase of cells in the domain and the decrease of the timestep, since the solver is explicit in time. Due to the absence of an initial RANS solution, the computations were initialized by performing four full rotations on an initial mesh (very coarse). The solution was then interpolated to the two meshes described above. For Cases 1 to 3, one extra rotation is enough to achieve unsteady convergence. Cases 4 and 5, capable to resolve more turbulent fluctuations, demand twice that time.

	Mesh	Timestep(sec)	SGS model	Cost
Case 1	MESH1	0.4e-7	Smago	6K
Case 2		0.4e-7	WALE	6K
Case 3		0.4e-7	Sigma	6K
Case 4	MESH2	5e-9	Smago	800K
Case 5		5e-9	WALE	800K

TABLE 4: SUMMARY OF THE CASES INVESTIGATED IN THIS STUDY

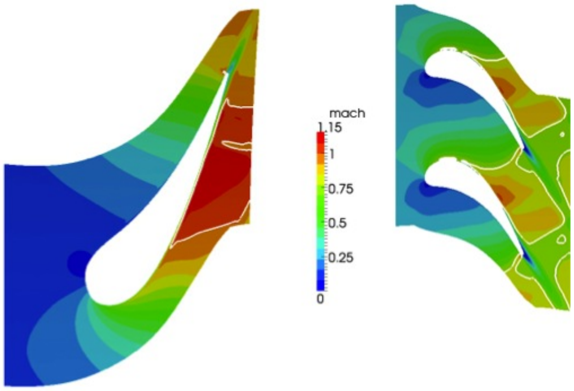

FIGURE 2: RELATIVE MACH NUMBER ACROSS THE STATOR (left) AND ROTOR BLADES (right)

RESULTS

Before analyzing the impact of models and mesh refinement, the main flow topology and unsteady secondary flows are described on the basis of the predictions from Case 1. Figure 2 depicts the relative, time-averaged, Mach number, M, in the stator and rotor domains respectively, along with a white contour of $M = 1$. On the stator suction side, the flow accelerates, reaches the speed of sound at the effective ”throat” of the blade passage and continues to accelerate as the passage diverges before the generation of a double shock. In the rotor, the behavior is similar with the flow also reaching transonic speeds. The difference lies in the shock structures observed, where a weak λ-type shock precedes a normal shock at the trailing edge.

Regarding secondary flows, the two principal ones observed in high-pressure turbine blades (both stator and rotor) are the hub and casing passage vortices, induced by the interaction of the incoming boundary layer at the endwalls and the pitchwise pressure gradient created by the blades. These are evident in both the stator and rotor blades on Fig. 3, which shows an isosurface of the Q criterion [35], colored by the local absolute Mach number. It can be seen that the vortices in the stator are small and stay closer to the endwalls. The rotor passage vortices, on the other hand, are stronger and expand more across the passage. These findings are in agreement with other URANS findings in similar configurations [36]. Additional flow structures, developing at the hub, the casing of the stator and at the hub of the rotor, are the horseshoe vortices. As the flow close to an endwall approaches a blade, it faces an adverse pressure gradient, leading to a small boundary layer separation and recirculation bubble. This forces the incoming flow to form small horseshoe vortices, which then interact with the main passage vortices [11, 37]. They are partly visible on Fig. 3 but due to their smaller size, increasing the mesh resolution at the endwalls is essential for a better capturing of the phenomenon. Focusing on the rotor blades only, an additional mechanism for creating secondary flows exists and is highlighted in Fig. 3. The presence of the tip clearance and the pressure difference between the pressure and suction side of the blade give rise to the tip leakage vortex, further down the chord of the blade.

Looking at Fig. 3 several interactions are also evident. The stator experiences vortex shedding at the trailing edge, which then impacts the rotor blade. The part of the wake that enters the suction side is quickly distorted and elongated structures are formed, which stay close to the suction side of the blade due to the pressure gradient in the passage. The tip passage vortex and the tip leakage vortex also interact, giving rise to a very unsteady wake close to the casing. Closer to the hub, the stator wake appears to interact strongly with the hub passage vortex of the rotor.

Effects of the sub-grid scale model

Figure 4 shows the time averaged isentropic Mach number across the stator vane for the three SGS models (Cases 1, 2 and 3) and for three different spans of the blade: 10,50 and 90%. All three models predict similar behaviors across both the pressure and suction side of the blade. Small differences exist close to the trailing edge at 10% span, where a hub corner vortex exists close to the trailing edge and the models predict a slightly different location of the separation point. At the other spans, the minor differences are related to the shock structures on the suction side. As confirmed by these results, experimental curves

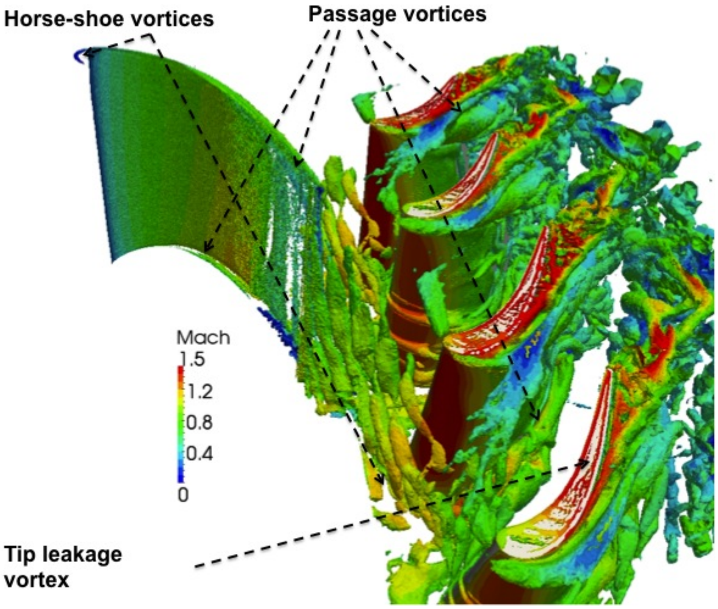

FIGURE 3: Q CRITERION OF AN INSTANTANEOUS SOLUTION ACROSS THE TURBINE STAGE

are successfully reproduced by these wall-modeled LES. Figure 5 depicts the mean Mach number across the stator for Cases 2 and 3. The biggest difference is the transformation of the double shock into a single shock close to the trailing edge. The reason for this change is the difference in the boundary layer thickness and the matching region with the law-of-the-wall model [23]. Indeed, the Smagorinsky model, by construction, has difficulty to reproduce the change of scales in the boundary layer and the expected elimination of turbulent viscosity as we approach the wall (property P1), which requires a specific damping function such as the Van Driest function [38]. However, this function demands an accurate calculation of the wall shear stress and is difficult to employ in complex geometries [39], thus it is not frequently employed in realistic configurations. The WALE and σ models, by construction, tend to respect this flow behavior and therefore help the use of law-of-the-wall. As evidenced in Fig. 5, both models are consistent and only minor differences are observed between Cases 2 and 3.

Similar findings are observed in the rotor. The pressure profiles across the blade at mid-span (Fig. 6a) reveal a shock on the suction side for Case 1, while Cases 2 and 3 show a smoother deceleration of the flow, sticking better to the experimental curves. This difference is evidenced through plots of the relative Mach number at mid-span for (Figs. 6b and 6c), where the weak λ shock of Case 1 (seen in the right part of Fig. 3) is no longer present and only the trailing edge shock remains.

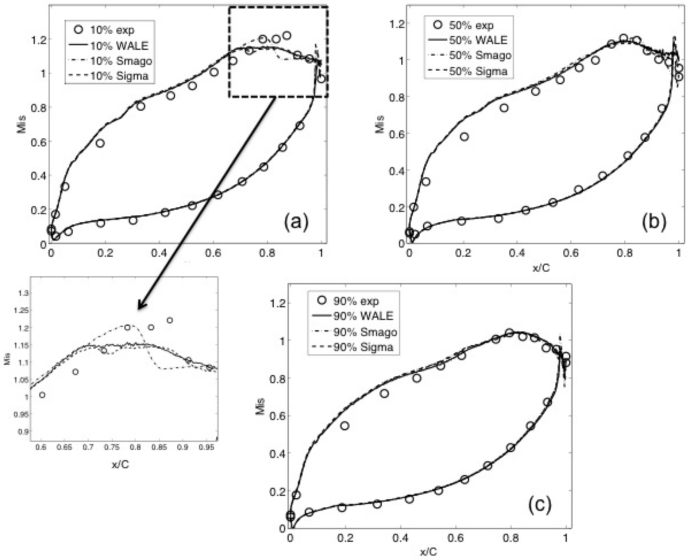

FIGURE 4: ISENTROPIC MACH NUMBER ACROSS THE STATOR AT 10% (a), 50% (b) and 90% SPAN

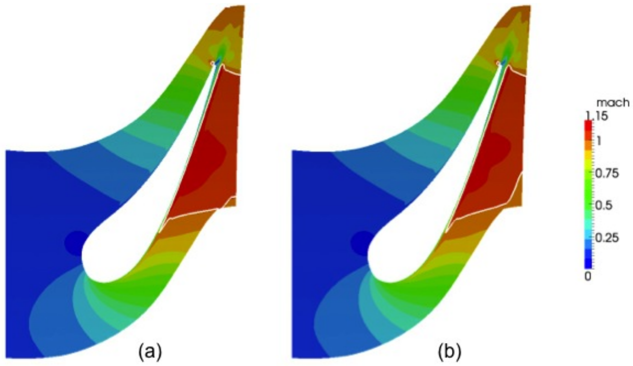

FIGURE 5: MACH NUMBER IN STATOR DOMAIN AT MID-SPAN FOR CASES 2 (a) AND 3 (b)

Looking at the density gradient ($\frac{||\nabla\rho||}{\rho}$) of the 3 cases across the flow field (Fig. 7) on an instantaneous solution (and at the same phase) allows to evaluate the acoustics content of the flow, shock structures and the blade wakes more clearly. In Fig. 7a the basic phenomena are highlighted, in order to facilitate the comparisons between the 3 cases. The stronger density gradients are generated by the shocks on the stator suction side (A), the shocks on the rotor suction side (B and C), a shock near the rotor trailing edge (D), and the vortex shedding and associated wave generation (D). The smaller levels of turbulent viscosity in Cases 2 and 3 permit a better representation of the acoustic waves produced by the interaction of the flow and the vortex shedding of the trailing edge of the stator (position E). These waves propagate and

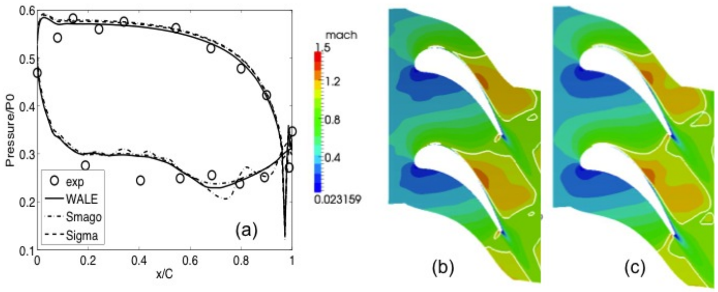

FIGURE 6: NORMALISED PRESSURE ACROSS THE ROTOR BLADE (a) AND RELATIVE MACH NUMBER AT MID-SPAN FOR CASES 2 (b) AND 3 (c)

impact the neighboring blades. For Case 2, this interaction leads to the creation of a small separation zone close to the trailing edge of the stator around mid-span, which is a known sensitivity of the wall-law combined with non-intrusive SGS models in near wall regions [40]. Case 3 appears to be the least intrusive behind the stator blade, hence permitting a clearer representation of the vortex shedding. However, the acoustic waves seem to have dissipated somewhat. In the rotor domain, the unsteady nature of the flow across the suction side can be highlighted by observing the differences in the shock strengths and their positions with respect to the stator wake. Looking at the previously highlighted positions, Position B (7) is on the suction side of a rotor blade that is being impacted by the stator's wake, while position C is on the suction side of a rotor that has overcome the impact of the wake. It is evident in all cases that when the wake impacts the rotor blade and propagates downstream, it changes the shock structure on the rotor suction side, as well as its strength.

Figure 8 shows azimuthally averaged radial profiles of several flow variables at the rotor exit in the near (less than 1 chord after the rotor trailing edge) and far field (approximately 3 chords). All cases show a good qualitative agreement with the experiments both in the near and far field. Differences observed close to the hub and close to the casing are due to the poorer grid resolution in these areas. Neither the hub nor the casing or tip clearance are adequately resolved with MESH1, hence creating a small shift of the curves close to the casing. It is also worth noting that in the far field the cell size is much larger than in the near field, thus degrading the quality of the results. Another issue is the wall boundary condition, taken as adiabatic in the simulations, while being isothermal in the experiment. This parameter mainly impacts the total temperature predictions, due to the absence of a thermal boundary layer in adiabatic simulations. Nonetheless, the predictions show improvement over previous RANS/URANS results [16], particularly in the flow reorientation (yaw angle). The difference observed in the levels of the Mach number at the rotor exit are linked to a small static pressure drift due to the non-reflecting boundary conditions employed. Qualitatively though, the trend is well captured. It is worth observing that while Cases 1 and 2 give similar predictions for the rotor's tip region in the near field, Case 3 shows a small shift, indicating that the secondary flow prediction is altered.

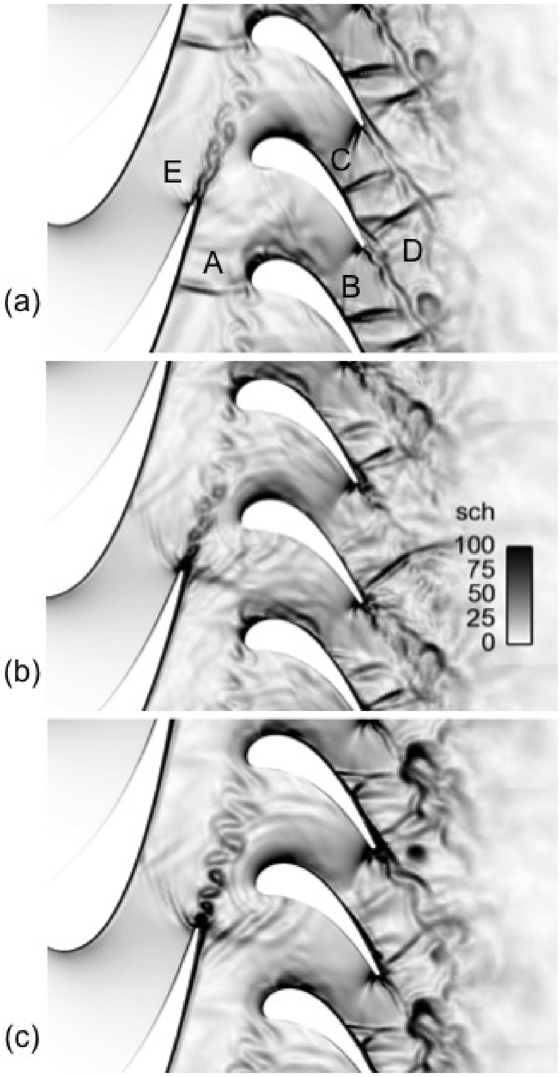

FIGURE 7: $\frac{||\nabla\rho||}{\rho}$ ACROSS THE TURBINE STAGE FOR CASES 1 (a), 2 (b) and 3 (c), INSTANTANEOUS SOLUTION

A good way to evaluate the differences in unsteady activity and turbulence content of the LES prediction is by measuring the azimuthally averaged resolved unsteadiness (Unsteadiness $= \frac{|\tilde{\mathbf{u}}'|}{\overline{\mathbf{U}}}$, where $|\tilde{u}'|$ is the magnitude of the resolved velocity fluctuations vector and $\overline{\mathbf{U}}$ is the magnitude of the mean velocity vector), Fig. 9. At the stator/rotor interface (Fig. 9a), it is evident that the

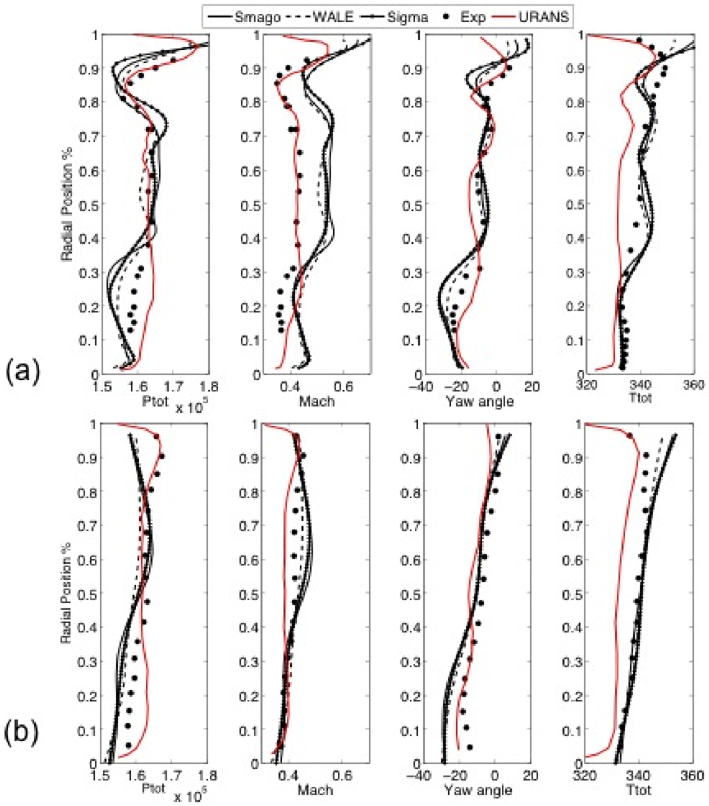

FIGURE 8: RADIAL PROFILES FOR CASES 1,2, 3 AND URANS [16] AT THE ROTOR EXIT (a) NEAR FIELD (b) FARFIELD

WALE and σ models show higher resolved activity than the Smagorinsky. The peak observed at the hub is related to the corner vortex located at the stator and at this span, while the slight increase in unsteadiness around mid-span (50-80% of the span) for the WALE model is related to the small separation occurring on the suction side before the trailing edge. At the rotor exit (Fig. 9b), different behaviors are observed near the tip, where using the Smagorinsky and the σ models depicts the highest level of activity. Such differences are clearly issued by the tip leakage vortex, which is highly sensitive to SGS modeling. In this region, where the boundary layer of the rotor blade, of the casing and the tip leakage vortex are in close proximity, each model impacts the flow differently and leads to differences between each flow field.

To get a better insight on the differences in the resolved turbulence between the three cases, a temporal probe, placed in the stator wake at mid-span and approximately 7mm behind its trailing edge in the main flow direction, is used. A PSD of the unsteady pressure signals is then performed and plotted in logarithmic scales (Fig. 10, cutoff frequency 450k Hz). All signals have a similar behavior and the $-5/3$ slope of the decay is captured.

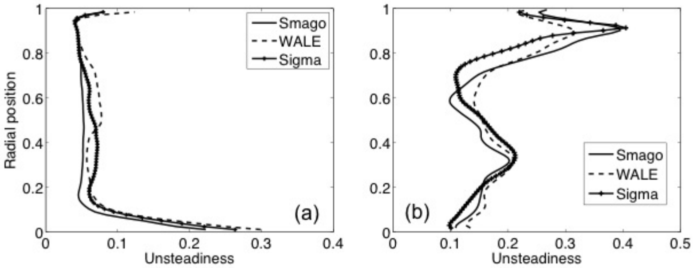

FIGURE 9: UNSTEADINESS AT ROTOR/STATOR INTERFACE (a) AND AT ROTOR EXIT (b)

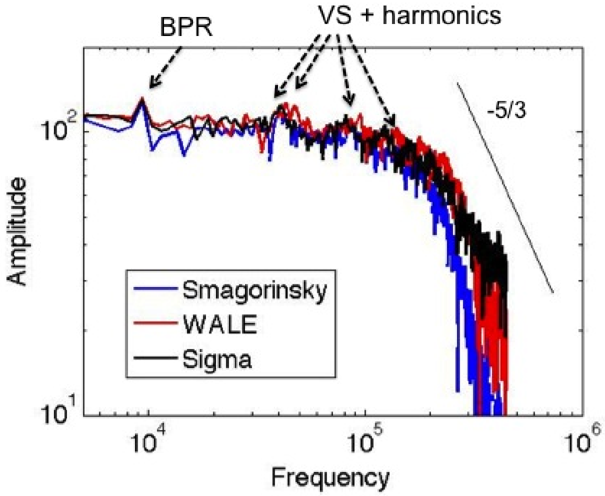

FIGURE 10: PSD OF THE TEMPORAL PRESSURE SIGNAL OF A PROBE IN STATOR'S WAKE

On top of this turbulent cascade of energy, several peaks appear related the rotor blade passing frequency (BPR), the vortex shedding from the stator trailing edge (VS), as well as harmonics of these frequencies. Cases 1 and 2 show the same vortex shedding frequency, while Case 3 predicts a wake with a slightly decreased frequency. Cases 2 and 3 have a larger amplitude and a larger range of frequencies with a pronounced linear slope all the way to the higher frequencies. This property, however, is not fully observed with the Smagorinsky model, which appears to be too dissipative. It can also be noted that the σ model shows saturation in the smaller scales, with the slope of the spectrum increasing slightly as the cutoff frequency is approached.

Effects of mesh resolution

For this part, four different cases from Table 4 are investigated. Cases 1 and 2 of the previous part serve as the basic low resolution simulations using the Smagorinsky and WALE model respectively, while the high resolutions Cases 4 and 5 are added. The objective is to investigate the impact of higher mesh resolution on the mean flow variables as well as on the general flow field and structure content. Since turbine flow is a wall-dominated flow with separations and reattachments, mesh under-resolution and modeling will alter the predictions. Increasing the mesh resolution allows to resolve more turbulent fluctuations and, ideally, a more accurate unsteady representation of the flow field is expected. Note that wall laws continue to be applied, since the maximum $y+$ measured places the first nodes in the beginning of the buffer region of a turbulent boundary layer.

Figure 11 shows the isentropic Mach number and normalized pressure across the stator and rotor blades respectively for the four cases. The differences between them are only minor and located mainly at the trailing edge of the stator at 10% span, where the hub corner vortex is present. It can be concluded that the mean pressure field is not significantly improved by the higher mesh resolution. Figure 12 compares the azimuthally averaged radial profiles at the rotor's exit. Both in the near and in the far field, there is general improvement over Cases 1 and 2, notably in the tip clearance region, where the number of cells has been increased from 6 to approximately 17 layers. The number of cells, however, is still insufficient and further refinement is necessary for more accurate predictions, which is in agreement with the findings of You et al [32]. Experimental trends are better captured in the far field (where previously the cell size was much bigger) and differences exist also in the total temperature profiles at the hub and casing with the appearance of a more realistic near wall profile.

While the mean pressure field reveals no significant changes, looking at the density gradient of an instantaneous solution for Cases 4 and 5 (Fig. 13(a) and 13(b) respectively) and comparing them to those of Cases 1 and 2 (in Fig. 7(a) and (b)) reveals important differences. Naturally, the decreased cell size allows for a much clearer representation of the vortex shedding of the stator blade and the acoustic wave generation. Additionally, Cases 1 and 4, which both use the Smagorinsky model, show the same shock structure but with different shock strengths (notably the shock on the stator suction side becomes weaker with the increasing mesh resolution). Case 5 exhibits a much stronger shock at the stator trailing edge, if compared to Case 2. Unsteady behavior of the rotor shock structures with respect to the stator's wake is still observed for all cases. A notable difference lies in the boundary layer thickness prediction. Case 4 depicts a boundary layer thickness similar to Case 1, while Case 5 shows a significantly reduced thickness. The Smagorinsky model's inability to adapt in the near-wall regions will alter the local Reynolds number, leading to similar predictions in the boundary layer for both the coarse and the fine mesh. For the WALE model the sensitivity of the wall-modeled approach to local resolution becomes evident.

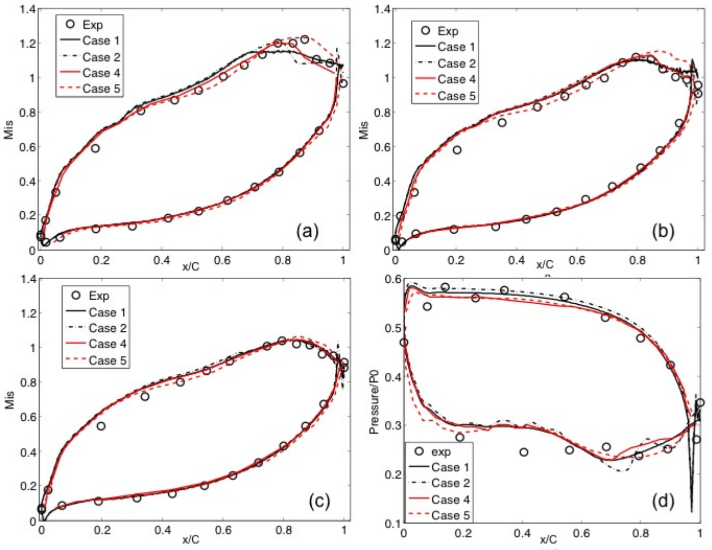

FIGURE 11: ISENTROPIC MACH NUMBER ACROSS STATOR BLADE AT 10% SPAN (a), 50% SPAN (b), 90% SPAN (c) AND NORMALISED PRESSURE ACROSS THE ROTOR BLADE AT 50% SPAN (d)

To look at the turbulence resolved with the fine mesh, Fig. 14 shows an isosurfaces of the Q-criterion, colored by the absolute Mach number. Comparing to Case 1 (Fig. 3), the difference in the resolved structures is clear. The higher resolution reveals a wealth of smaller turbulent structures. The main flow features remain the same, with the elongated structures appearing on the rotor suction side, as well as the hub, tip passage vortices and the tip leakage vortex. The stator wake, however, is no longer represented by a clear pattern. The main vortices have finer turbulent structures wrapped around them, indicating a rapid transition to a fully turbulent flow. Another difference lies in the tip vortices, which appear to be constrained to higher radius. It is interesting to note that the tip clearance area is characterized by finer structures. Looking at the differences between Cases 4 and 5, it is evident that Case 4 shows larger and fewer structures, while Case 5 has a larger number of finer ones. This again relates to higher turbulent viscosity values for Case 4, hence, a lower effective Reynolds number of the flow. This result is coherent with the conclusions of the previous section and indicates that the Smagorinsky model is not adapted for turbine flows.

CONCLUSIONS

Several LES of the high-pressure experimental turbine MT1 have been performed to evaluate the effect of sub-grid scale models and mesh resolution in a wall-modeled rotor-stator LES. Mean results show qualitative agreement with the experiments

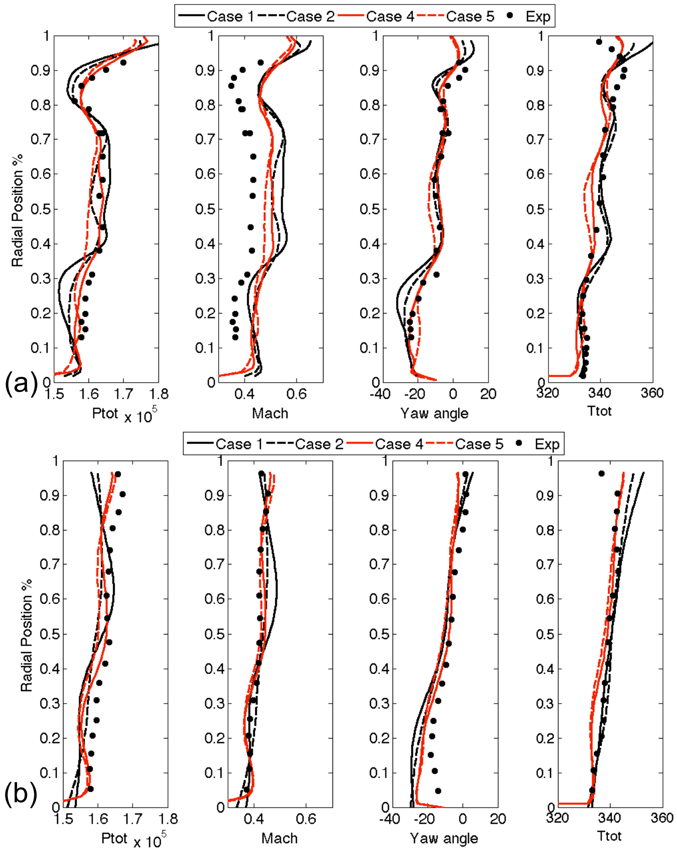

FIGURE 12: ROTOR EXIT PROFILES IN NEAR (a) AND FAR (b) FIELD

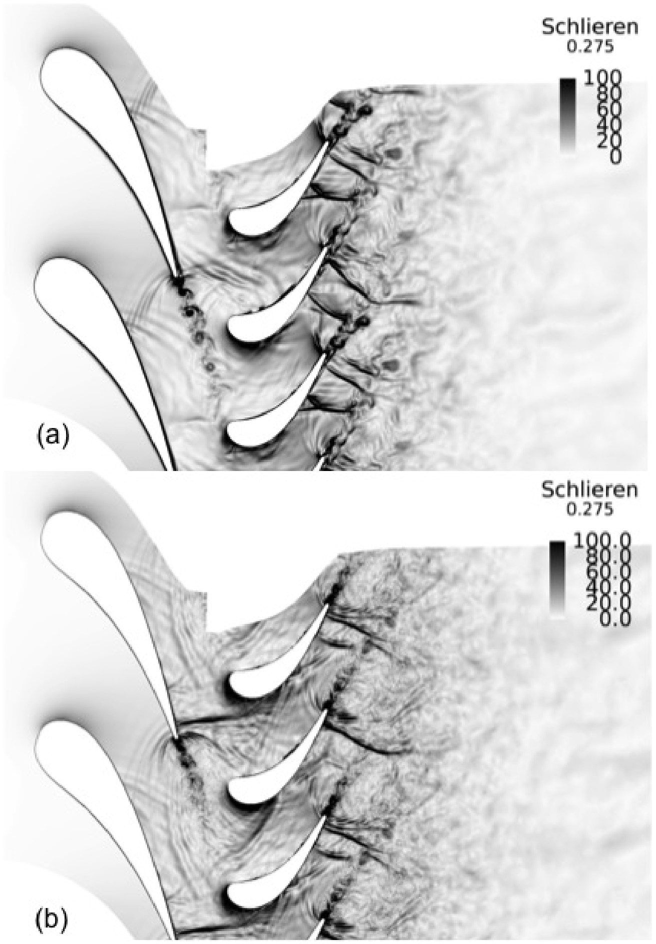

FIGURE 13: DENSITY GRADIENT AT MID-SPAN FOR CASES 4 (a) AND 5 (b)

performed at the Oxford Turbine Research facility for all cases and some improvement over URANS results from Beard et al [16] is evidenced. However, an important sensitivity of LES predictions to different modeling parameters is revealed here. It is shown that sub-grid scale models, with their different characteristics, lead to different flow fields characterized by different shock structures and unsteady contents, particularly when used with a coarse mesh. Using a sub-grid scale model adapted to wall-bounded flows predicts a flow with higher unsteadiness and a higher effective turbulent Reynolds number. Increasing the mesh resolution shows minor changes on the mean flow predictions. However, decreasing the cell size of the mesh and improving near wall resolution, combined with a model adapted for near-wall regions, not only increases the level of turbulent structures but also changes the boundary layer thickness and near-wall dynamics. The unphysical behavior of the Smagorinsky model close to walls prevents the latter effect to appear and the unsteadiness in the flow remains lower than with the WALE model. Future work will need to exploit more the high resolution cases in order to provide a reference for future simulations. Another issue still to be addressed is the introduction of more accurate inlet boundary conditions that include realistic turbulent fluctuations with adequate length scales. Further refinement on the endwalls is also necessary to better capture secondary flows.

ACKNOWLEDGMENT

The author gratefully acknowledges the funding from the European Community's Seventh Framework Programme (FP7, 2007-2013), under the grant agreement No. FP7-290042 (COPA-GT project). The author would also like to thank Dr. Nicolas Gourdain for the fruitful discussions. Finally, the authors are grateful to Safran Turbomeca and the consortium of the TATEF-II project for providing access to the data of the MT1 turbine.

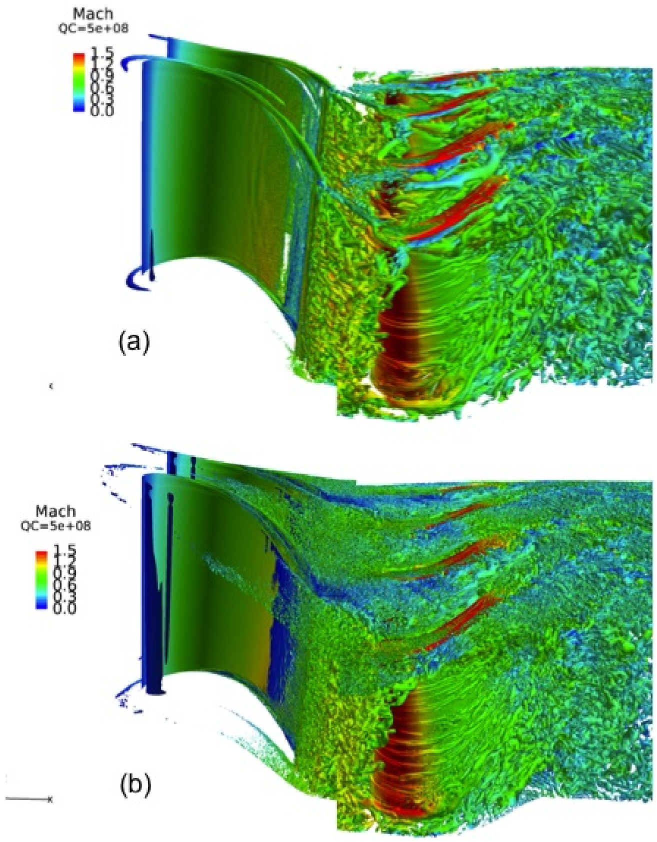

FIGURE 14: Q CRITERION COLOURED BY MACH NUMBER FOR CASES 4 (a) AND 5 (b)

REFERENCES

[1] Tucker, P., 2011. "Computation of unsteady turbomachinery flows: Part 2-LES and hybrids". *Progress in Aerospace Sciences,* ***47***, pp. 546–569.

[2] Menzies, K., 2009. "Large eddy simulation applications in gas turbines". *Philosophical Transactions of the Royal Society,* ***367***, pp. 2827–2838.

[3] Jenkins, S., and Bogard, D., 2005. "The effects of the vane and mainstream turbulence level on hot streak attenuation". *Journal of Turbomachinery,* ***127***, pp. 215–221.

[4] Collado-Morata, E., Gourdain, N., Duchaine, F., and Gicquel, L., 2012. "Structured vs unstructured les for the prediction of free-stream turbulence effects on the heat transfer of a high pressure turbine profile". *Journal of Heat and Mass Transfer,* ***55***(21-222), pp. 5754–5768.

[5] Chapman, D., 1979. "Computational aerodynamics development and outlook". *AIAA Journal,* ***17***(12), pp. 1293–1313.

[6] Michelassi, V., Wissink, J., Froehlich, J., and Rodi, W., 2003. "Large eddy simulation of flow around low-pressure turbine blade with incoming wakes". *AIAA Journal,* ***41***(11), pp. 2143–2156.

[7] Wu, X., and Durbin, P., 2001. "Evidence of longitudinal vortices evolved from distorted wakes in a turbine passage". *Journal of Fluid Mechanics,* ***446***, pp. 199–228.

[8] Raverdy, B., Mary, I., Sagaut, P., and Liamis, N., 2004. "High-resolution large-eddy simulation of flow around low-pressure turbine blade". *AIAA Journal,* ***41***(3), pp. 390–397.

[9] Gomar, A., Gourdain, N., and Dufour, G., 2011. "High fidelity simulation of the turbulent flow in a transonic axial compressor". In European Turbomachinery Conference.

[10] You, D., Mittal, R., Wang, M., and Moin, P., 2003. "Study of a rotor tip-clearance flow using large eddy simulation". In Proceedings of 41th Aerospace Science Meeting and Exhibit, no. AIAA-2003-0838.

[11] Lampart, P., 2009. "Investigation of endwall flows and losses in axial turbines. part 1: Formation of endwall flows and losses". *Journal of theoretical and applied mechanics,* ***47***(2), pp. 321–342.

[12] Gourdain, N., 2013. "Validation of large-eddy simulation for the prediction of compressible flow in an axial compressible stage". In Proceedings of the ASME Turbo Expo 2013 Gas Turbine Technical Congress and Exposition, no. GT2013-94550.

[13] McMullan, W., and Page, G., 2012. "Towards large eddy simulation of gas turbine compressors". *Progress in Aerospace Sciences,* ***52***, pp. 30–47.

[14] Wang, G., Papadogiannis, D., Duchaine, F., Gourdain, N., and Gicquel, L., 2013. "Towards massively parallel large eddy simulation of turbine stages". In Proceedings of the ASME Turbo Expo 2013 Gas Turbine Technical Congress and Exposition, no. GT2013-64852.

[15] Schoenfeld, T., and Rudgyard, M., 1999. "Steady and unsteady flow simulations using the hybrid flow solver avbp". *AIAA Journal,* ***37***, pp. 1378–1385.

[16] Beard, P., Smith, A., and Povey, T., 2011. "Experimental and computational fluid dynamics investigation of the efficiency of an unshrouded transonic high pressure turbine". *Journal of Power and Energy,* ***225***, pp. 1166–1179.

[17] Salvadori, S., Montomoli, F., Martelli, F., Adami, P., Chana, K., and Castillon, L., 2011. "Aerothermal study of the unsteady flow field in a transonic gas turbine with inlet temperature distortions". *Journal of Turbomachinery,* ***133***.

[18] Hosseini, S., Fruth, F., Vogt, D., and Gransson, T., 2011. "Effect of scaling of a blade row sectors on the prediction of aerodynamic forcing in a highly-loaded transonic turbine stage". In Proceedings of the ASME Turbo Expo 2011 Gas Turbine Technical Congress and Exposition, no. GT2011-45813.

[19] Hilditch, M., Fowler, A., Jones, T., Chana, K., Oldfield, M., Ainsworth, R., Hogg, S., Anderson, S., and Smith, G.

"Installation of a turbine stage in the pyestock isentropic light piston facolity". No. ASME paper no. 94-GT-277.

[20] Qureshi, I., Beretta, A., Chana, K., and Povey, T., 2011. "Effect of aggresive inlet swirl on heat transfer and aerodynamic in an unshrouded transonic hp turbin". In Proceedings of the ASME Turbo Expo 2011 Gas Turbine Technical Congress and Exposition, no. GT2011-46038.

[21] Sagaut, P., 2002. *Large eddy simulation for incompressible flows*. Springer.

[22] Nicoud, F., Baya-Toda, H., Cabrit, O., Bose, S., and Lee, J., 2011. "Using singular values to build a subgrid-scale model for large eddy simulations". *Physics of Fluids,* ***23***(8).

[23] Bocquet, S., Sagaut, P., and Jouhaud, J., 2012. "A compressible wall model for large eddy simulation with application to prediction of aerothermal quantities". *Physics of Fluids,* ***24***(065103).

[24] Smagorinsky, J., 1963. "General circulation experiments with the primitive equations, i. the basic experiment". *Monthly Weather Review,* ***91***, pp. 99–164.

[25] Nicoud, F., and Ducros, F., 1999. "Subgrid-scale modelling based on the square of the velocity gradient tensor". *Flow, Turbulence and Combustion,* ***62***, pp. 183–200.

[26] Germano, M., Piomelli, U., Moin, P., and Cabot, W., 1991. "A dynamic sub-grid scale eddy viscosity model". *Physics of Fluids,* ***A***(3), pp. 1760–1765.

[27] Duchaine, F., Jaure, S., Poitou, D., Quemerais, E., Staffelbach, G., Morel, T., and Gicquel, L., 2013. "High performance conjugate heat transfer with the openpalm coupler". In V International Conference on Coupled Problems in Science and Engineering.

[28] Moureau, V., Lartigue, G., Sommerer, Y., Angelberger, C., Colin, O., and Poinsot, T., 2005. "Numerical methods for unsteady compressible multi-component reacting flows on fixed and moving grids". *Journal of Computational Physics,* ***202***(2), pp. 710–736.

[29] Lax, P., and Wendroff, B., 1964. "Difference schemes for hyperbolic equations with high order of accuracy". *Communications on pure and applied mathematics,* ***17***, pp. 381–398.

[30] Colin, O., and Rudgyard, M., 2000. "Development of high-order taylor-galerkin schemes for unsteady calculations". *Journal of Computational Physics,* ***162***(2), pp. 338–371.

[31] Beard, P., Smith, A., and Povey, T., 2011. "Impact of severe temperature distortion on turbine efficiency". In Proceedings of the ASME Turbo Expo 2011 Gas Turbine Technical Congress and Exposition, no. GT2011-45647.

[32] You, D., Mittal, R., Wang, M., and Moin, P., 2004. "Computational methodology for large eddy simulation of tip-clearance flows". *AIAA Journal,* ***42***(2), pp. 271–279.

[33] Poinsot, T., and Lele, S., 1992. "Boundary conditions for direct simulations of compressible viscous flows". *Journal of Computational Physics,* ***101***, pp. 104–129.

[34] Koupper, C., Poinsot, T., Gicquel, L., and Duchaine, F., 2013. "On the ability of characteristic boundary conditions to comply with radial equilibrium in turbomachinery simulations". *submitted to AIAA Journal*.

[35] Haller, G., 2005. "An objective definition of a vortex". *Journal of Fluid Mechanics,* ***525***, pp. 1–26.

[36] Wlassow, F., 2010. "Analyse instationnaire aérothermique d'un etage de turbine avec transport de points chauds; application a la maitrise des performances des aubages". PhD thesis, Ecole Centrale Lyon.

[37] Sharma, O., and Butler, T., 1987. "Predictions of endwall losses and secondary flows in axial flow turbine cascades". *Journal of Turbomachinery,* ***109***(2), pp. 229–236.

[38] Driest, E. V., 1956. "On turbulent flow near a wall". *Journal of Aerospace Sciences,* ***23***, pp. 1007–1011.

[39] Leveque, E., Toschi, F., Shao, L., and Bertoglio, J.-P., 2007. "Shear-improved smagorinsky model for large-eddy simulation of wall-bounded turbulent flows". *Journal of Fluid Mechanics,* ***570***, pp. 491–502.

[40] Jaegle, F., Cabrit, O., Mendez, S., and Poinsot, T., 2010. "Implementation methods of wall functions in cell-vertex numerical solvers". *Flow, Turbulence and Combustion,* ***85***(2), pp. 245–272.